npj | 2D materials and applications

Article

Published in partnership with FCT NOVA with the support of E-MRS

https://doi.org/10.1038/s41699-026-00677-2

Oxide induced degradation in MoS_2 field-effect transistors

Fabian Ducry[1] ✉, Benoit Van Troeye[1], Mauro Dossena[2], Mathieu Luisier[2], Geoffrey Pourtois[1] & Aryan Afzalian[1] ✉

Transition Metal Dichalcogenides (TMDC) are promising candidates for future scaled transistor channels but their performance is often degraded by imperfections such as the interface with amorphous gate oxides. This study examines how amorphous Al_2O_3 and HfO_2 interfaces affect monolayer to trilayer MoS_2 transistors using first principles simulations. We link atomic-scale features of their surfaces to experimentally observed performance degradation in TMDC device performance. Our findings show that atomic-scale variations of the dielectric environment cause potential fluctuations in the TMDC that reduce mobility and drive current while increasing subthreshold swing (SS) in short channel devices. Additionally, surface defects in the oxides introduce gap states that act as traps, causing source-to-drain leakage currents and further SS degradation. Notably, mobility drops less in trilayer than in mono- and bilayer MoS_2, consistent with experiments showing that thicker layers are more resilient to oxide-induced performance degradation. Nonetheless, monolayer MoS_2 models with homogeneous, defect-free amorphous oxide surfaces can retain up to 80% of the on-current of an ideal crystalline oxide. These insights help optimize oxide interfaces to preserve device performance in TMDC-based transistors.

Two-dimensional (2D) materials are a class of layered crystals with great promise as semiconducting channels for future scaled integrated CMOS field-effect transistors (FETs)[1,2]. Transition Metal Dichalcogenides (TMDCs), in particular, have been extensively studied. Their high density of states and intrinsic mobilities are expected to be maintained down to the single layer limit[3]. Additionally, they are predicted to be robust to short channel lengths effects[4]. These characteristics render them prime candidates for short-channel Complementary Metal-Oxide Semiconductor (CMOS) devices, where thin channels are required for an adequate gate control.

This ultimate channel thickness scaling amplifies the importance of interfaces between the channel and its surrounding dielectrics as the surface-to-volume ratio peaks[5]. In silicon, the existence of a high quality thermal native oxide between the channel and the insulating gate oxide alleviates this challenge because of its low defect density, low roughness, and high chemical uniformity[6]. The most widely studied high quality gate oxide for 2D FETs is crystalline hexagonal Boron Nitride (h-BN). Inserted between the channel and the CMOS gate oxide, it screens oxide-induced potential fluctuations and preserves the intrinsic mobility of TMDCs[7,8]. While h-BN offers excellent interface quality, its low dielectric constant limits its use in ultra-scaled devices, which motivates interest in high-κ amorphous oxides. Currently, uniformly depositing and growing high-κ oxides on 2D materials is challenging[2,9,10]. As a result, underwhelming channel mobilities are widespread in large-scale integrated 2D FETs[11]. Oxide-induced performance degradation remains a key challenge to broad adoption of 2D materials in integrated electronics.

Intrinsically, single layer MoS_2 can outperform bilayer and trilayer MoS_2 in terms of mobility[12]. In contrast, integrated devices with a full gate stack show the reverse trend. Experimental studies observed that reducing the thickness of the TMDC channel leads to a decrease in the device mobility[13–16]. This decrease is partly attributed to stronger influence of the oxide surface, emphasizing the need to understand and mitigate interface-induced degradation in ultra-thin channels. Several hypotheses have been proposed to explain the origin of the oxide-induced degradation. These include long-ranged oxide remote-phonon scattering[17], oxide surface defects[5,18,19], fluctuating dielectric environment due to surface roughness or inhomogeneous termination[20], or oxide-induced corrugation of the 2D material[21]. A precise understanding of these mechanisms is crucial to improve channel mobility in integrated 2D FETs. Quantum transport studies of TMDCs, so far, have focused on free-standing 2D materials or treated imperfections as parametric inputs such as trap states and surface charges[22–24]. Consequently, they depend on assumptions about degradation and parameter fitting.

[1]Imec, 3001 Leuven, Belgium. [2]Integrated Systems Laboratory (IIS), ETH Zurich, 8092 Zurich, Switzerland. ✉e-mail: fabian.ducry@imec.be; aryan.afzalian@imec.be

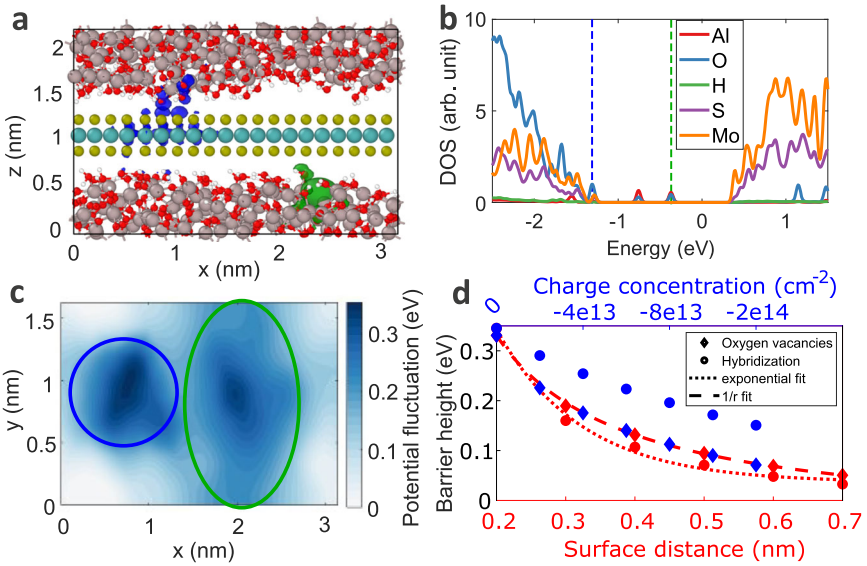

Fig. 1 | Defects at the MoS_2/am-Al_2O_3 interface. **a** Visualization of a MoS_2/am-Al_2O_3 interface model. The isosurface of the molecular orbital originating from one of the oxygen vacancies and the hybridization are shown in green and blue, respectively. **b** Projected density of states of the unit cell in (**a**). The Fermi energy is at 0 eV. Two oxygen vacancies create gap states between −1 eV and 0 eV, the hybridization a valence tail state at −1.3 eV. The vertical dashed green and blue lines indicate the energy levels of the orbitals in (**a**). **c** Oxide-induced potential fluctuations in the Mo layer. The line barrier on the right is due to oxygen vacancies (green oval), the localized dot on the left to the hybridization (blue circle). **d** Peak potential fluctuations due to oxygen vacancies (diamonds) and hybridization (dots) as a function of the MoS_2/am-Al_2O_3 distance r (red) and extra charge density in the MoS_2 (blue). The lines show the 1/r (dashed) and exponential (dotted) fitting to the data.

First-principles electronic structure simulations require no material parameters or experimental fitting. Thus, they are an emerging tool to investigate large-scale surfaces and interface-related properties to complement experimental activities. Several density functional theory (DFT) based modeling studies of device-scale structures have been demonstrated, often in conjunction of multiscale approaches[25–28]. Key challenges include limited experimental knowledge of the atomistic morphology and nature of said interfaces, especially for amorphous materials, and the high computational cost. Thus, most theoretical 2D/oxide interfaces studies focus on crystalline systems[29], except for our recent works, which have examined the impact of am-Al_2O_3 and am-HfO_2 on the electronic structure of monolayer (ML) WS_2[30] and the mobility of ML WS_2[8]. The first of latter two studies discusses the construction and ground-state properties of interfaces between amorphous oxides and ML WS_2. The second one uses non self-consistent Non-equilibrium Green's Function formalism (NEGF) simulations to investigate the low-field mobility degradation in ML WS_2 with am-Al_2O_3 under long channel, near equilibrium conditions and discusses the benefit of an interfacial h-BN layer.

The present work uses fully self-consistent NEGF simulations to directly link oxide surface features to device-level degradation in mono- to trilayer MoS_2 FETs. We compute device mobilities, current-voltage (I-V) characteristics, subthreshold swings (SS), and ON-current (I_{ON}) and evaluate how amorphous oxides exacerbate short-channel effects. Interface electronic structures are obtained from DFT and transistor performance is evaluate using NEGF-based quantum transport simulations. We use MoS_2 as channel material, a prime 2D n-FET candidate[2]. For gate oxides we consider the industrially relevant am-Al_2O_3 and am-HfO_2, explicitly included in our atomistic models. First, we examine the thickness scaling from ML to trilayer (TL) MoS_2 with am-Al_2O_3. Second, we compare three interfaces to explore short channel ML and bilayer (BL) MoS_2 n-FET prospects. By correlating oxide surface features with device characteristics, we show that oxide-induced potential fluctuations grow and mobility decreases as MoS_2 gets thinner, and provide insight into gate oxide induced 2D FET performance degradation. These results match experimental mobility trends which decrease with MoS_2 channel thickness due to dielectric factors[16].

Results and discussion

Interface characteristics

Figure 1a illustrates one of the ML MoS_2/am-Al_2O_3 atomistic interface model we have investigated in this work. For information on how the models have been generated and computational details, we refer to the Methods section. The MoS_2 is free from defects and there is a gap between the materials, which are held together by weak dispersive forces. Two kinds of imperfections can be identified from the electronic structure of this interface model: (1) localized states in the band gap of MoS_2, and (2) orbitals that hybridize between the oxide surface and MoS_2. One of each kind is visualized in Fig. 1a by the green and blue isosurfaces, respectively.

The gap states can be readily identified in the projected density of states (PDOS) in Fig. 1b. In this MoS_2/am-Al_2O_3 interface, the two gap states arise due to oxygen vacancies (V_O) 0.76 eV and 1.15 eV below the conduction band minimum, respectively. One is located at the lower oxide surface (shown in Fig. 1a) and the other is deeper in the am-Al_2O_3, resulting in an interface trap density (D_{IT}) of 4e13 cm^{-2}. Am-Al_2O_3 is reported to introduce a D_{IT} in MoS_2, matching this density[31]. The occupation probability of gap states is given by the Fermi energy. Experimentally, am-Al_2O_3 is often reported to induce n-type doping in TMDCs[32,33], indicating that the Fermi energy should also be close to the conduction band. Consequently, gap states have a high probability to be occupied.

In this model, the gap states from Fig. 1a are charged. This locally modifies the electrostatic potential, thereby inducing a barrier in the neighboring MoS_2. The electrostatic potential energy in the Mo layer of the unit cell, which was extracted from the diagonal of the Kohn-Sham matrix exported from DFT cf. Methods, is shown in Fig. 1c, where a barrier originating from the two V_O is clearly visible. Due to the close proximity of the V_O and limited width of the unit cell, the barriers from both V_O combine to form a line barrier with a maximum height of 340 meV.

The hybridization between MoS_2 and am-Al_2O_3 originates from the non-uniform oxide surface termination. The two surfaces are close enough that a mixing of electronic states may occur in the presence of a local charge imbalance at the oxide surface. The orbital shown in blue in Fig. 1a is such a hybridized state and is projected to 41% on Mo, 31% on S, 26% on O, and 2% on Al, despite the minimal distance of 2.48 Å between S and O. Similar to the charged V_O, hybridization induces a potential energy barrier in the MoS_2, as shown in Fig. 1c. The barrier from the hybridization is spatially separated from the V_Os and forms a single peak with a height of 360 meV.

The PDOS of the sapphire/MoS_2 interface is shown in Supplementary Fig. 3b for reference. It reveals that the valence band maximum of the MoS_2 also hybridizes with the sapphire and 16% of the orbital is projected onto O. Crucially, however, the hybridization is homogeneous through the unit cell, cf. Supplementary Fig. 3a, and does not locally perturb the potential energy.

Together, the combination of the barriers generated from the charged V_O and the hybridization results in potential fluctuations in the MoS_2. Its

fingerprint is unique to each oxide surface and sensitive to oxide defects and local surface termination, as will be explored in a later section.

Artificially increasing the separation (r) between the surfaces reduces potential fluctuations, as illustrated in Fig. 1d (bottom axis). The peak height from the hybridization (red dots) rapidly drops before tapering off. The one from the charged V_O (red diamonds) exhibits a more gradual reduction. We hypothesize that the barrier from charged V_O follows a 1/r-dependence due to its origin from a localized charge (dashed red line). As the hybridization between the two materials is a density effect, we expect it to follow an exponential decay (red dotted line). The top axis in Fig. 1d shows the peak potential fluctuation with increasing charge density in the MoS_2. Analogously to increasing interface distance, the barrier from V_O is screened by charge in MoS_2, following the same trend (blue diamonds). The screening is quite effective due to the spatial separation of the V_O from the MoS_2 by a van der Waals gap. The barrier from hybridization, however, shows a weaker dependency to charge screening. This is most likely because the defect density is partially located in the MoS_2 itself and therefore cannot be effectively suppressed.

Device degradation

We correlate the oxide-induced electronic property changes to device performance through DFT-NEGF simulations. The double gate 2D n-FET that is used to evaluate the effect of the gate dielectric is schematically shown in Fig. 2a. It is composed of periodically repeated unit cells of the am-Al_2O_3/MoS_2 structure in Fig. 1a. We use a channel length (L_{CH}) of 5 nm and an equivalent oxide thickness (EOT) of 0.5 nm such that short channel effects are clearly visible. Source and drain are 26.5 nm long with a doping of 2e13 cm^{-2} per layer. A source-drain voltage (V_{DS}) of 0.4 V is used to keep the computational burden of the simulations manageable (cf. Methods for more details).

Our simulations assume an infinite (periodic) channel width. In practice, scaled CMOS devices, however, rely on nanosheet and nanoribbon architectures, where edge effects such as roughness and disorder are important and can dominate mobility degradation[34–36]. The physical insights into oxide-induced degradation remain relevant for these architectures, and we expect that both effects would likely coexist and further degrade mobility.

Figure 2b shows the I-V curves of a 2D n-FET with am-Al_2O_3. As reference, we also show crystalline Al_2O_3 (sapphire). Four major changes are caused by the am-Al_2O_3 as compared to sapphire: (1) increased source-to-drain leakage current at low gate bias (V_{GS}), (2) a plateau in the subthreshold regime, (3) an increase in SS, and (4) a reduction of the saturation current.

The additional leakage at low V_{GS} that is visible in the 2D n-FET with am-Al_2O_3 (1) is due to trap-assisted tunneling (TAT). At this V_{GS}, the energy of the highest gap state from Fig. 1b gets aligned with the energy of the conduction band minimum in the source contact, which allows for tunneling through this state. (2) is due to charging of this gap state. It is unoccupied when $V_{GS} < 0.0$ V, while it is fully charged above 0.15 V. The spectral electron density at 0.1 V V_{GS} is depicted in Fig. 2c, where this defect state in two consecutive unit cells just below the energy of the drain is visible. In between it is progressively charged, giving rise to the potential energy barrier visible in Fig. 1c. The increasing potential fluctuations partially compensate for the reduction of the channel barrier due to increased V_{GS} and pins the maximum channel barrier height. These V_O can act as interface traps, or manifest in random telegraph noise (RTN), both of which are observed experimentally[31,37,38]. The gate voltage at which source-to-drain leakage and barrier pinning occurs heavily depends on the position of the gap state with respect to the band edges. We expect that the local environment of a V_O determines its position in the band gap, and hence a broad distribution of interface traps from amorphous materials. The two gap states in this model are already 390 meV apart.

The am-Al_2O_3 also increases the SS (3) above the TAT and barrier pinning regions. We extract a SS of 95 meV/dec and 70 meV/dec at 50 nA/μm for am-Al_2O_3 and sapphire, respectively. This increase stems from the potential fluctuations, which alter the shape of the channel barrier in the subthreshold regime. Figure 2d shows two different examples of effective channel barriers that arise from the potential fluctuations of the am-Al_2O_3 model, depending on their alignment with the macroscopic

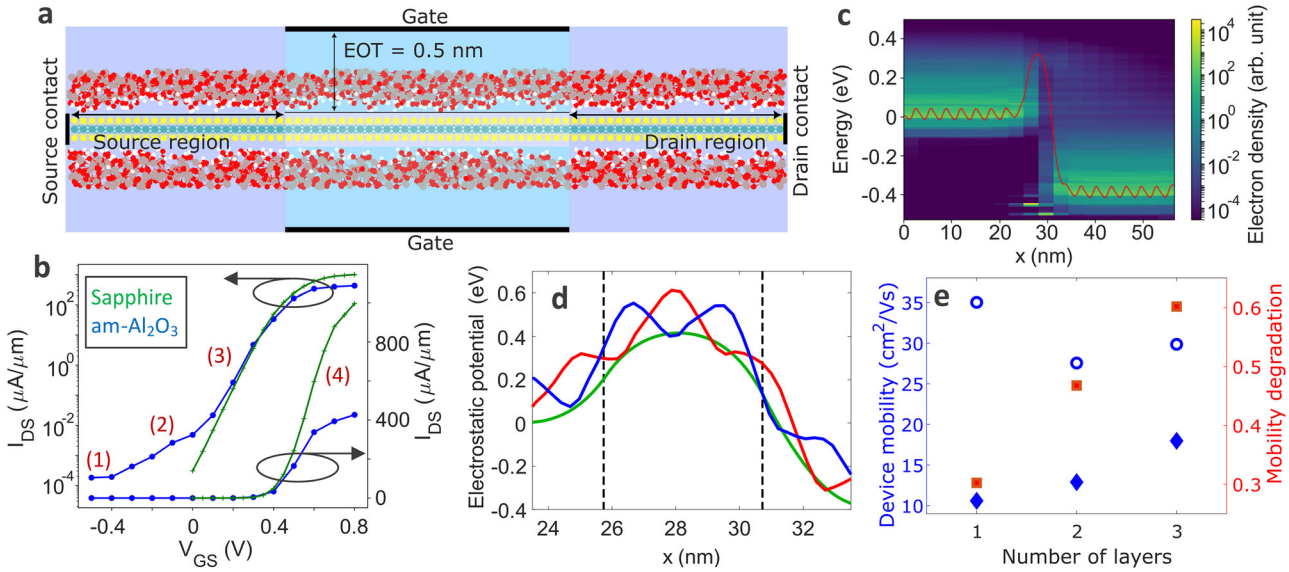

Fig. 2 | Device simulation of MoS_2 with am-Al_2O_3 and sapphire. a Visualization of the 2D double gate n-FET structure used to evaluate the impact of amorphous oxides on MoS_2. The green and yellow spheres mark Mo and S atoms, the red, gray, and white ones O, Al, and H, respectively. The blue shaded area represents the macroscopic gate oxide with an EOT of 0.5 nm and a gate contact at the top and bottom of it. The source and drain regions are 26.5 nm long (not to scale) with a doping of 2e13 cm^{-2} per layer. **b** I-V curves for sapphire (green) and am-Al_2O_3 (blue) gate dielectrics with 0.5 nm effective oxide thickness at 5 nm channel lengths and 0.4 V V_{DS}. (1)–(4) indicate TAT, barrier pinning, increased SS, and reduced saturation current. **c** Spectral electron density of the device in (**a**) at 0.1 V V_{GS}. The red line marks the macroscopic electrostatic potential energy. **d** Channel barrier of the MoS_2 n-FET in (**a**) at 0.4 V V_{DS} and 0.0 V V_{GS} for sapphire (green), am-Al_2O_3 (blue), and am-Al_2O_3 shifted by half a unit cell (red). For am-Al_2O_3, the barrier is the sum of the potential fluctuations and macroscopic electrostatic potential energy. The vertical dashed black lines indicate the boundaries of the channel. **e** Device mobility (left axis) at V_{GS} 0.6 V versus channel thickness with sapphire (blue circles) and am-Al_2O_3 (blue diamonds). The right axis (red squares) shows the ratio of the mobilities at the respective thickness.

channel barrier. Various effects can happen, e.g., wells can form and act as tunneling or hopping centers, or the width of the barrier can be reduced. They all lessen the capability of the channel to block electrons from leaking from source to drain. Thus, they decrease the effective length of the channel and increase the SS. Additionally, the potential fluctuations induce a shift of the threshold voltage (V_{th}) which can lead to device-to-device variability.

Varying the effective channel barrier by changing the spatial alignment of the channel and potential fluctuations (Fig. 2d) has an impact on device characteristics such as SS and I_{ON}. For a fixed OFF-current (I_{OFF}) at 10 nA/μm, we found a variation of 40 meV/dec in the SS and 10% of I_{ON} at 0.6 V V_{GS}. This fact indicates that amorphous oxides can induce considerable device-to-device variability at short channel lengths. Lastly, potential fluctuations cause carriers to be scattered (4) and thereby decrease the electrical current. This correlates with the reduction of the saturation current due to am-Al_2O_3.

The device mobility at 0.6 V V_{GS} is shown in Fig. 2e for mono- to trilayer MoS_2 for a channel length of 20 nm. The mobility is consistently lower in the presence of am-Al_2O_3 as compared to crystalline sapphire. However, the degradation increases with decreasing channel thickness. The apparent mobility at 0.6 V V_{GS} decreases by 70%, 53%, and 40% due to the the am-Al_2O_3, respectively. This result is in line with experimental observations that device mobilities in MoS_2-based FETs decrease with channel thickness[16].

Surface comparison

The magnitude of oxide degradation depends on the surface morphology and not all degradation mechanisms are necessarily present at every interface to the same degree. Furthermore, the potential fluctuations change with the number of MoS_2 layers constituting the 2D channel. We examined these effects on three surface models, M1 and M2 with am-Al_2O_3 and M3 with am-HfO_2. Additionally, we compared ML and BL MoS_2 interfaced with each of the three amorphous oxides.

Figure 3a shows the potential fluctuations in MoS_2 induced by each surface model for ML and BL MoS_2. The raw data for all six structures can be found in the supporting information in Supplementary Fig. 1. Figure 3b quantifies these fluctuations by reporting (i) the maximum amplitude within the unit cell and (ii) the minimum barrier, as indicated by the black lines and arrow in Fig. 3a. The minimum-barrier height serves as an indicator of percolation across the unit cell: the larger the barrier, the more energy an electron needs for a continuous percolation path.

M1 is the model in Fig. 1. Its average distance between the oxide and the S from MoS_2 is 3.1 Å, see Table 1. The root-mean square deviation from the average distance (RMS) is 0.59 Å, indicating some atomic scale roughness of the surface. Additionally, the nearest neighbor species for each S atom is recorded. In M1, 97 S atoms have H as their nearest neighbor, giving a H coverage of 81% of the surface, with the reminder of S being exposed to O. ML M1 shows two distinct features of the potential fluctuation in Fig. 3a: a localized peak due to hybridization and a broad barrier due to charged V_O with a maximum height of 360 meV and 340 meV, respectively. Additionally, electrons face a minimal barrier height of 85 meV to cross the unit cell. In bilayer MoS_2, the impact from the V_O appears in both layers but at reduced magnitude of 210 meV and 220 meV in each layer. The hybridization affects the bottom layer with a peak height of 180 meV. The minimal barrier height also decreases from 85 meV in ML to 64 meV BL.

The average interface distance of M2 is 2.9 Å with a RMS of 0.34 Å. The H coverage is 61% and there are even 5 Al atoms that are exposed to the S. Compared to M1, the oxide surface has less roughness but also less H passivation. The potential fluctuations in M2 originate from two hybridization sites, one at each surface, see Supplementary Fig. 1b, e. In ML MoS_2 the peak heights are 200 meV and 240 meV while in the BL they are 380 meV and 410 meV, one in each layer. The minimal barrier height increases from 103 meV in ML to 171 meV in BL MoS_2. The potential energies averaged over y and z are similar for the ML and BL, as shown in Supplementary Fig. 1b, but the energies in the individual layers of the BL deviate considerably (Supplementary Fig. 1e). The smaller potential fluctuation peaks in ML indicate that the potential modulations induced by both oxide interfaces average out to some degree. The electrostatic coupling between the two layers in BL MoS_2, however, seems to be quite low, such that the averaging from the ML does not come to effect.

The average interface distance of M3 is 2.9 Å with a RMS of 0.45 Å. The average distance is the same as M2 and the roughness of M3 lies between M1 and M2. With a H coverage of 91%, M3 is better passivated than both M1 and M2. The hybridization between MoS_2 and the oxide is weaker in M3 than in the previous models, with a peak barrier height of 200 meV and 140 meV in ML and BL, respectively. Furthermore, there is no minimal barrier for electrons to overcome in order to cross this unit cell. For further analysis and discussion of the surface termination we refer the interested reader to ref. 30.

The six models are then used as the constituting building elements of double-gate 2D n-FETs. For each device, I_{ON} and SS are computed for L_{CH} ranging from 5 nm to 14.4 nm, and reported in Fig. 4a–d. We fixed I_{OFF} at 10 nA/μm per device, in line with the IEEE IRDS target[39], and extracted I_{ON} at 0.6 V V_{GS}. Consequently, I_{ON} combines oxide degradation and short-channel effects. The SS reported here is the average slope between V_{GS} = 0.0 V and 0.2 V. The full I-V curves for the devices with 6.6 nm and 15 nm L_{CH} can be found in Supplementary Fig. 4.

I_{ON} decreases for shortening L_{CH} in all devices, especially below 8 nm (see Fig. 4a, b), including the ones with sapphire as gate oxide. The reduction of I_{ON} due to the amorphous oxide is reported in Fig. 4e, f for ML and BL, respectively. M1 and M2 perform similarly for the ML with a current reduction in between 60% and 70% with respect to sapphire. For BL MoS_2, M1 performs better than the ML, with a reduction of roughly 50%. M2, on the other hand, suffers from the large potential fluctuations which reduce the current by 80%. M3 consistently performs better, with 70% to 80% on-current retention with respect to sapphire for the ML and BL, respectively. This demonstrates that it is theoretically possible to preserve 2D n-FET performance even in the presence of amorphous gate oxides. The I_{ON} reduction is far more pronounced in ML M2 than M3, despite similar maximum potential fluctuations of 240 meV and 200 meV, respectively. The absence of a minimal barrier in M3 (100 meV in M2) indicates that a percolation path is readily available in M3 but absent in M2.

Both ML and BL MoS_2 suffer from SS degradation below 8 nm and 10 nm channel lengths, respectively, even with sapphire as gate oxide. However, the effect is more pronounced in BL MoS_2 due to reduced gate control in the thicker channel region. In M1 (ML) and M2, the SS degradation with respect to sapphire (ΔSS) is accentuated by the gate oxide, as seen from the increase of SS in Fig. 4g, h. At 5 nm L_{CH} we record ΔSS of 41 mV/dec and 31 mV/dec for ML M1 and BL M2, respectively, correlating with the largest potential fluctuations as shown in Fig. 3b. The SS of ML M1 even surpasses the one of the BL with 114 mV/dec and 106 mV/dec, respectively. Similar to I_{ON}, M3 suffers from little SS degradation with respect to sapphire, reinforcing the fact that amorphous gate oxides do not necessarily degrade MoS_2 n-FETs, if its surface is sufficiently homogeneous and free of defects.

The diagram provided in Fig. 5 summarizes the impact of amorphous oxides on ML and BL MoS_2. It links the simulated device degradations to the associated mechanisms and traces them to their electronic origin in the atomistic model of am-Al_2O_3 or am-HfO_2 and MoS_2.

Based on our computations, we traced the leakage down to trap-assisted tunneling enabled by gap states due to surface oxygen vacancies. The increase of the SS originates from potential fluctuations induced oxide gap states which can pin the barrier in the subthreshold regime, or create Coulomb barriers. Moreover, inhomogeneities at the oxide surface lead to hybridization with MoS_2 which also contribute to the potential fluctuations and impact the SS. Fluctuating electrostatic potential in the MoS_2 due to the amorphous oxide inhomogeneity causes scattering of carriers and substantially reduces the saturation current.

In detail, we have identified two distinct contributions to potential fluctuations in our models. These are oxide defects and hybridization

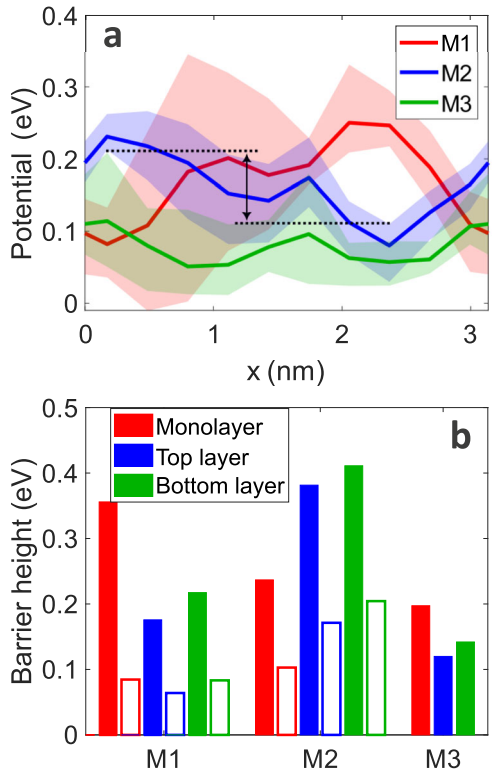

Fig. 3 | Potential fl uctuations induced in MoS_2. a Potential fluctuations induced by the models M1–M3 in monolayer MoS_2. The solid lines mark the average over the cross-section, while the shaded areas outline the range of calculated potential energy. The black dashed lines and arrow indicate the minimal barrier height of M2. **b** Barriers induced by the potential fluctuations in M1–M3 and for mono- and bilayer MoS_2. The solid bars indicate the maximum amplitude of the potential fluctuations. The empty bars indicate the minimum barriers.

between the oxide and MoS_2. The latter originate from interactions between the oxide surface atoms and MoS_2, and are caused by local imbalances in the surface termination. In our models, this mainly correlates with the hydrogen coverage. The larger it is, the lower the potential fluctuations in the adjacent MoS_2.

Oxide defects came in the form of oxygen vacancies in our structures. These tend to form localized defect states with energy levels in the band gap of MoS_2. As such, they act as centers for trap-assisted tunneling. Moreover, in case of n-type doping, which is typically reported for am-Al_2O_3, they are charged and contribute significantly to the potential fluctuations.

Degradation summary

We constructed three interfaces of MoS_2 with amorphous Al_2O_3 or HfO_2 (M1–M3) to examine impacts of surface termination and native oxide defects on 2D n-FET performance. M1 reproduces the experimentally observed thickness-dependent mobility degradation, which increases from TL to down ML, highlighting the impact of oxide-induced potential fluctuations[16]. Amorphous gate oxides can increase source-to-drain leakage currents, raise subthreshold swings, and reduce saturation currents. A clean interface is therefore critical to preserve the electrical performances of the 2D materials.

M3's high hydrogen coverage yields a homogeneous surface with little hybridization and no oxygen-vacancy defects. M2 has comparatively little hydrogen at its surface and exhibits strong hybridization. M1 has intermediate hydrogen coverage but two charged oxygen vacancies with gap states. Consequently, n-FETs with M3 clearly outperform M1 and M2, delivering up to 80% of the performance of crystalline sapphire. Surface roughness appears secondary here, possibly masked by the stronger effects of hybridization and oxygen vacancies.

Table 1 | Structural surface properties of our M1–M3 models

	Surface distance		Nearest neighbor species		
	Average	RMS	H	O	M
M1	3.1 Å	0.59 Å	97	23	0
M2	2.9 Å	0.34 Å	73	42	5
M3	2.9 Å	0.45 Å	109	11	0

The first column lists the average distance between each S atom of monolayer MoS_2 and its nearest neighbor from the oxide. The root-mean square deviation from the average distance (RMS) is given in column two. Columns three to five count the nearest neighbor oxide surface species for each S atom for ML MoS_2. M denotes the metal species of the oxide, Al in M1 and M2, Hf in M3.

This work underscores the need for uniform and defect-free oxide surfaces for optimal 2D n-FET performance. Quantitative oxide surface studies of their defects and terminations are critical to identify optimal gate oxides for integrated 2D CMOS logic devices. We assumed an EOT of 0.5 nm for all models. Surface treatments to lower the potential fluctuations in MoS_2 might affect the oxides permittivity. Hence, evaluating the surfaces impact on EOT should also be of utmost priority. Lastly, we assumed ideal phonons as in free-standing MoS_2 due to computational limits. However, oxides are expected to impact phonon properties as well as electronic ones: either by modifying intrinsic phonons in MoS_2, or remote polar phonon scattering. Assessing these effects will also facilitate the optimization of 2D channel - gate oxide interfaces.

Methods

DFT calculation

The DFT calculations were performed with the CP2K software package version 9.1[40]. We employed the PBEsol[41] functional combined with Grimme's DFT-D3(BJ) dispersion correction with Becke–Johnson damping[42,43]. The dispersion correction is crucial for the description of interface between MoS_2 and the passivated surface of am-Al_2O_3 or am-HfO_2. We used double-zeta valence polarized (DZVP) MOLOPT basis sets on all chemical species except for Mo, where a triple-zeta valence polarised (TZVP) basis was used. This combination of basis sets was found to produce band structures in excellent agreement with the plane-wave code VASP, see Supplementary Fig. 2. Spin-orbit coupling was not included explicitly in the DFT calculations, only through the scalar relativistic GTH pseudopotentials[44]. Its effect on the conduction band of MoS_2 is small, hence we expect little impact on the n-type transport considered in this work[45]. The Brillouin zone is sampled with a single k-point located at the zone-center, as motivated by the large cross-section of the MoS_2 layer and the amorphous nature of the oxide.

The unit cell includes the interface between MoS_2 and the gate oxide. It measures 3.1 nm × 1.6 nm. The in-plane lattice parameters were fixed to the one of free-standing ML MoS_2 to prevent oxide induced strain which would complicate the comparison between models[46]. For BL MoS_2 AB-stacking was considered. The interface models between the MoS_2 and amorphous oxides were obtained using the combination of decorate-and-relax method[47,48], and a surface construction scheme as proposed by Van Troeye et al.[30]. The model M1 corresponds to the roughcut in ref. 30, M2 to a modified version of the sharpcut-4x, and M3 a variant of the am-HfO_2 model from the same reference. Both M2 and M3 were changed to be fully stoichiometric such that there is neither H excess or shortage. This greatly facilitates the convergence of quantum transport simulations. Additionally, the WS_2 used in ref. 30 was replaced by MoS_2. After these changes were introduced, the structures were optimized with DFT such that the amorphous network could find an optimal configuration, with a pressure tolerance of 100 bar, a force tolerance of 0.45 mHa/Bohr, and a maximum step size of 0.003 Bohr.

Potential fluctuations

To compute the potential fluctuations, we subtracted the diagonal elements of the orthogonalized Kohn-Sham matrices with and without the oxide and then averaged over the entries per atom. Thus, the potential fluctuations

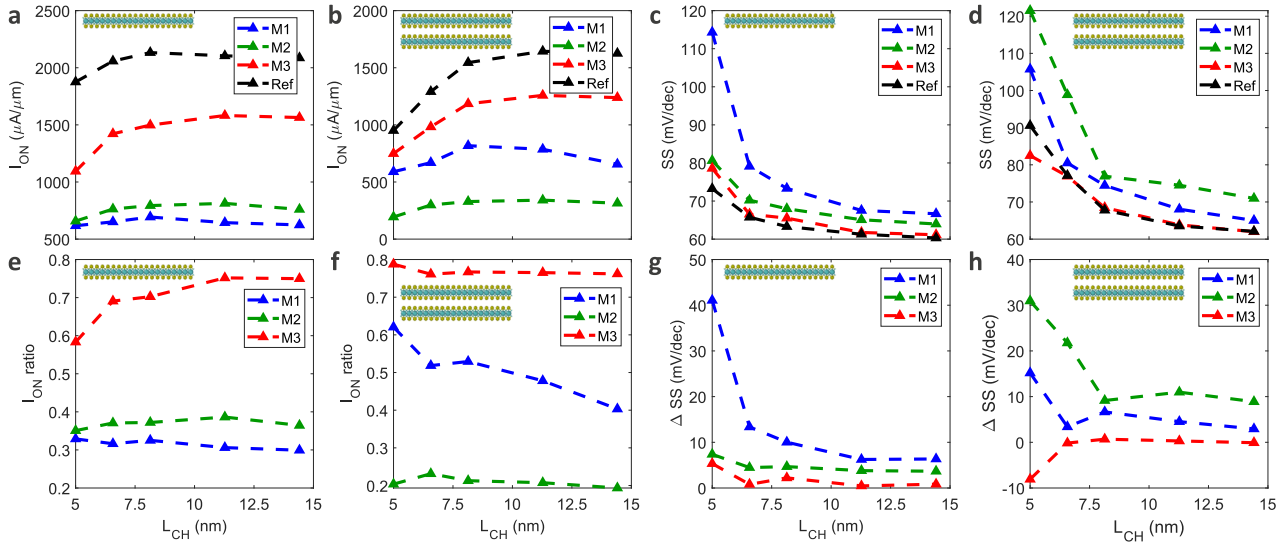

Fig. 4 | Device performance with diff erent oxides. Insets depict one or two layers of MoS2 indicating whether the data corresponds to ML or BL. **a** On-current (I_{ON}) for the M1, M2, and M3 shown in Fig. 3 plus sapphire with monolayer MoS_2. **b** Same as (**a**) but with bilayer MoS_2. **c**, **d** Subthreshold swing of the devices in (**a**) and (**b**), respectively. **e**, **f** Reduction of I_{ON} due to amorphous oxide, quantified as the ratio of I_{ON} for M1, M2, M3 to that of sapphire, for mono- and bilayer MoS_2, respectively. **g**, **h** Increase of the subthreshold swing of M1 to M3 with respect to sapphire for mono- and bilayer MoS_2, respectively.

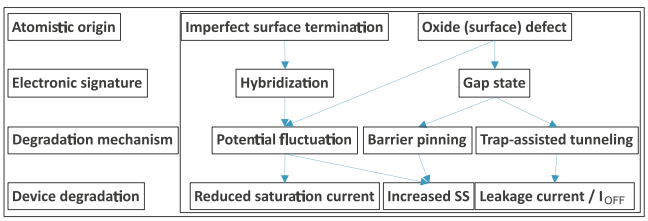

Fig. 5 | Degradation mechanisms from amorphous oxides. Diagram summarizing the degradation mechanisms observed in Fig. 1 and their influence on key figures of merits as illustrated in Fig. 2.

contain all local contributions from DFT. Moreover, it matches how the macroscopic potential is applied in the self-consistent NEGF-Poisson procedure.

Quantum transport

For the quantum transport simulations we use our in-house NEGF solver ATOMOS[4]. The NEGF-Poisson equations are solved self-consistently to obtain the macroscopic electrostatic potential. It should be noted that this includes effects from charging interface traps and electrodes. The source and drain contacts are ohmic with an n-type doping concentration of 2e13 cm^{-2}, which is added as a background charge when solving the Poisson's equation. The gate is implemented as a Dirichlet boundary condition for Poisson with a metal work function of 0.5 eV relative to the conduction band minimum of the MoS_2. Electron-phonon scattering is included through the self-consistent Born approximation within the deformation potential theory. We used the parameters derived for free-standing ML MoS_2 by Huang et al.[49]. Remote oxide phonons are proposed to be one of the mechanisms degrading transport in TMDCs and including them could potentially impact scattering in MoS_2[17]. However, deriving related parameters for amorphous oxides is currently beyond computational capability.

As Hamiltonian for the NEGF equation we used the Kohn-Sham and overlap matrices computed by CP2K. To export the Hamiltonian we used a combination of smaller basis sets with DZVP MOLOPT on Mo, S, and H, as well as single-zeta valence (SZV) MOLOPT on Al and O. Using the smaller basis does not impact the band structure of MoS_2 close to the conduction band edges and the position of defect levels is within 50 meV. Hence, the basis did not significantly affect the transport of n-type devices as studied here. Additionally, a mode space transformation was used to further reduce the dimension of the Hamiltonian and hence the computational burden[50,51]. The effectiveness of the mode space transformation decidedly depends on the energy window where transport takes place. To keep said energy window as small as possible, it was necessary to restrict V_{DS} to 0.4 V.

Mobility

The mobility values and reduction are computed from the device current (I_{DS}) and the charge density (n_{CH}) in the middle of the channel at $V_{GS} = 0.6$ V according to $\mu = L_{CH}{*}I_{DS}/(V_{DS}{*}n_{CH})$.

Data availability

Data sets generated for this publication are available from the corresponding author on reasonable request. All DFT input coordinates are provided as Supplementary Data.

Received: 15 October 2025; Accepted: 5 February 2026;
Published online: 11 March 2026

References

1. Lemme, M. C., Akinwande, D., Huyghebaert, C. & Stampfer, C. 2d materials for future heterogeneous electronics. *Nat. Commun.* **13**, 1392 (2022).
2. O'Brien, K. P. et al. Process integration and future outlook of 2d transistors. *Nat. Commun.* **14**, 6400 (2023).
3. Poncé, S., Royo, M., Gibertini, M., Marzari, N. & Stengel, M. Accurate prediction of hall mobilities in two-dimensional materials through gauge-covariant quadrupolar contributions. *Phys. Rev. Lett.* **130**, 166301 (2023).
4. Afzalian, A. Ab initio perspective of ultra-scaled CMOS from 2D-material fundamentals to dynamically doped transistors. *npj 2D Mater. Appl.* **5**, 5 (2021).
5. Knobloch, T. et al. Improving stability in two-dimensional transistors with amorphous gate oxides by fermi-level tuning. *Nat. Electronics* **5**, 356–366 (2022).
6. Morita, M., Ohmi, T., Hasegawa, E., Kawakami, M. & Ohwada, M. Growth of native oxide on a silicon surface. *J. Appl. Phys.* **68**, 1272–1281 (1990).

7. Lan, H.-Y., Tripathi, R., Appenzeller, J. & Chen, Z. Near-ideal subthreshold swing in scaled 2D transistors: the critical role of monolayer hBN passivation. *IEEE Electron Device Lett.* **45**, 1337–1340 (2024).
8. Dossena, M. et al. Mobility calculation in disordered WS_2-Al_2O_3 stacks from first principles. *npj 2D Mater. Appl.* **9**, 67 (2025).
9. Dorow, C. J. et al. Gate length scaling beyond Si: Mono-layer 2d channel FETs robust to short channel effects. In *2022 International Electron Devices Meeting (IEDM)*, 7.5.1–7.5.4 (IEEE, 2022).
10. Yang, S. et al. Gate dielectrics integration for 2d electronics: challenges, advances, and outlook. *Adv. Mater.* **35**, 2207901 (2023).
11. Wan, Y. et al. Low-defect-density WS_2 by hydroxide vapor phase deposition. *Nat. Commun.* **13**, 4149 (2022).
12. Lembke, D., Allain, A. & Kis, A. Thickness-dependent mobility in two-dimensional MoS_2 transistors. *Nanoscale* **7**, 6255–6260 (2015).
13. Li, S.-L. et al. Thickness-dependent interfacial coulomb scattering in atomically thin field-effect transistors. *Nano Lett.* **13**, 3546–3552 (2013).
14. Schmidt, H., Giustiniano, F. & Eda, G. Electronic transport properties of transition metal dichalcogenide field-effect devices: surface and interface effects. *Chem. Soc. Rev.* **44**, 7715–7736 (2015).
15. Yu, Z. et al. Analyzing the carrier mobility in transition-metal dichalcogenide MoS_2 field-effect transistors. *Adv. Funct. Mater.* **27**, 1604093 (2017).
16. Rai, A. et al. Progress in contact, doping and mobility engineering of MoS_2: an atomically thin 2D semiconductor. *Crystals* **8**, 316 (2018).
17. Gopalan, S., Van de Put, M. L., Gaddemane, G. & Fischetti, M. V. Theoretical study of electronic transport in two-dimensional transition metal dichalcogenides: effects of the dielectric environment. *Phys. Rev. Appl.* **18**, 054062 (2022).
18. Dean, C. R. et al. Boron nitride substrates for high-quality graphene electronics. *Nat. Nanotech.* **5**, 722 (2010).
19. Rhodes, D., Chae, S. H., Ribeiro-Palau, R. & Hone, J. Disorder in van der Waals heterostructures of 2d materials. *Nat. Mater.* **18**, 541–549 (2019).
20. Raja, A. et al. Dielectric disorder in two-dimensional materials. *Nat. Nanotechnol.* **14**, 832–837 (2019).
21. Shin, B. G. et al. Indirect bandgap puddles in monolayer MoS_2 by substrate-induced local strain. *Adv. Mater.* **28**, 9378–9384 (2016).
22. Long, Y. et al. Effect of lattice defects on electronic structure and thermoelectric properties of 2D monolayer MoS_2. *Phys. E Low. Dimensional Syst. Nanostruct.* **161**, 115972 (2024).
23. Xiao, Z., Guo, R., Zhang, C. & Liu, Y. Point defect limited carrier mobility in 2d transition metal dichalcogenides. *ACS Nano.* **18**, 8511–8516 (2024).
24. Rawat, A. & Rawat, B. The role of interface trap states in MoS_2 -FET performance: a full quantum mechanical simulation study. *IEEE Trans. Electron Devices* **70**, 4913–4920 (2023).
25. Cantele, G. et al. Structural relaxation and low-energy properties of twisted bilayer graphene. *Phys. Rev. Res.* **2**, 043127 (2020).
26. Ducry, F., Aeschlimann, J. & Luisier, M. Electro-thermal transport in disordered nanostructures: a modeling perspective. *Nanoscale Adv.* **2**, 2648–2667 (2020).
27. Leconte, N., Javvaji, S., An, J., Samudrala, A. & Jung, J. Relaxation effects in twisted bilayer graphene: a multiscale approach. *Phys. Rev. B* **106**, 115410 (2022).
28. Aeschlimann, J. et al. Multiscale modeling of metal-oxide-metal conductive bridging random-access memory cells: from ab initio to finite-element calculations. *Phys. Rev. Appl.* **19**, 024058 (2023).
29. Singh, A. K., Hennig, R. G., Davydov, A. V. & Tavazza, F. Al_2O_3 as a suitable substrate and a dielectric layer for n-layer MoS_2. *Appl. Phys. Lett.* **107**, 053106 (2015).
30. Van Troeye, B. et al. Impact of interface and surface oxide defects on WS_2 electronic properties from first principles. *ACS Nano.* **19**, 11664–11674 (2025).
31. Mootheri, V. et al. Interface admittance measurement and simulation of dual gated CVD WS_2 MOSCAPS: Mapping the D_{it}(E) profile. *Solid State Electron.* **183**, 108035 (2021).
32. You, Y. G. et al. Atomic layer deposited Al_2O_3 passivation layer for few-layer WS_2 field effect transistors. *Nanotechnology* **32**, 505702 (2021).
33. Piacentini, A. et al. Stable Al_2O_3 encapsulation of MoS_2-FETs enabled by CVD grown h-BN. *Adv. Electron. Mater.* **8**, 2200123 (2022).
34. Zhang, F., Lee, C.-H., Robinson, J. A. & Appenzeller, J. Exploration of channel width scaling and edge states in transition metal dichalcogenides. *Nano Res.* **11**, 1768–1774 (2018).
35. Chen, S., Zhang, Y., King, W. P., Bashir, R. & Van Der Zande, A. M. Edge-passivated monolayer WSe_2 nanoribbon transistors. *Adv. Mater.* **36**, 2313694 (2024).
36. Hoque, M. A. et al. Ultranarrow semiconductor WS_2 nanoribbon field-effect transistors. *Nano Lett.* **25**, 1750–1757 (2025).
37. Ravichandran, H. et al. Observation of rich defect dynamics in monolayer MoS_2. *ACS Nano.* **17**, 14449–14460 (2023).
38. Panarella, L. et al. Evidence of contact-induced variability in industrially-fabricated highly-scaled MoS_2 fets. *npj 2D Mater. Appl.* **8**, 44 (2024).
39. International Roadmap for Devices and Systems (IRDS) 2023 Edition. https://irds.ieee.org/editions/2023 Accessed 16-Feb-2026 (2023).
40. Kühne, T. D. et al. CP2K: an electronic structure and molecular dynamics software package - Quickstep: Efficient and accurate electronic structure calculations. *J. Chem. Phys.* **152**, 194103 (2020).
41. Perdew, J. P. et al. Restoring the density-gradient expansion for exchange in solids and surfaces. *Phys. Rev. Lett.* **100**, 136406 (2008).
42. Grimme, S., Anthony, J., Ehrlich, S. & Krieg, H. A consistent and accurate ab initio parametrization of density functional dispersion correction (DFT-D) for the 94 elements H-Pu. *J. Chem. Phys.* **132**, 184103 (2010).
43. Grimme, S., Ehrlich, S. & Goerigk, L. Effect of the damping function in dispersion corrected density functional theory. *J. Comput. Chem.* **32**, 1456 (2010).
44. Goedecker, S., Teter, M. & Hutter, J. Separable dual-space Gaussian pseudopotentials. *Phys. Rev. B* **54**, 1703–1710 (1996).
45. Molina-Sánchez, A., Sangalli, D., Hummer, K., Marini, A. & Wirtz, L. Effect of spin-orbit interaction on the optical spectra of single-layer, double-layer, and bulk MoS_2. *Phys. Rev. B* **88**, 045412 (2013).
46. Petö, J. et al. Moderate strain induced indirect bandgap and conduction electrons in MoS_2 single layers. *npj 2D Mater. Appl.* **3**, 39 (2019).
47. Drabold, D. A. Topics in the theory of amorphous materials. *Eur. Phys. J. B* **68**, 1–21 (2009).
48. Youn, Y., Kang, Y. & Han, S. An efficient method to generate amorphous structures based on local geometry. *Comput. Mater. Sci.* **95**, 256–262 (2014).
49. Huang, Z., Zhang, W. & Zhang, W. Computational search for two-dimensional MX2 semiconductors with possible high electron mobility at room temperature. *Materials* **9**, 716 (2016).
50. Shin, M., Jeong, W. J. & Lee, J. Density functional theory based simulations of silicon nanowire field effect transistors. *J. Appl. Phys.* **119**, 154505 (2016).
51. Afzalian, A. et al. Physics and performances of III-V nanowire broken-gap heterojunction TFETs using an efficient tight-binding mode-space NEGF model enabling million-atom nanowire simulations. *J. Phys. Condensed Matter.* **30**, 254002 (2018).

Acknowledgements

We thank Ruishen Meng and Michel Houssa for the VASP calculations to benchmark the basis sets in CP2K. We thank Cesar Javier Lockhart de la Rosa and Gouri Sankar Kar discussions on experimental and 2D integration aspects. The authors acknowledge the Imec Industrial Affiliation Program (IIAP) for funding. M.D. and M.L. acknowledge support from the NCCR MARVEL funded by the Swiss National Science Foundation under Grant No. 205602.

Author contributions

F.D., B.V.T., M.L., A.A., and G.P. conceived the project. F.D. performed the density functional theory and quantum transport calculations. B.V.T. constructed the atomistic supercells. B.V.T. and A.A. supervised the simulations and provided methodological guidance. F.D. wrote the original draft. F.D., B.V.T., M.D., M.L., A.A., and G.P. discussed and interpreted the results and contributed to writing—review & editing of the manuscript.

Competing interests

The authors declare no competing interests.

Additional information

Supplementary information The online version contains supplementary material available at https://doi.org/10.1038/s41699-026-00677-2.

Correspondence and requests for materials should be addressed to Fabian Ducry or Aryan Afzalian.